Journal of Operation and Automation in Power Engineering

vol. 13, no. Special Issue, Dec. 2025, Pages: 1-16

http://joape.uma.ac.ir

Research Paper

Enhanced Stability in Microgrids Using an Optimized Virtual Synchronous Generator Control for Voltage Source Converters

Mohammed Obayes Yousif , *Hassan Moradi* *, and *Hamdi Abdi*

Department of Electrical Engineering, Razi University, Kermanshah, Iran.

Abstract— *This study introduces a Virtual Dynamic Emulation–Virtual Synchronous Generator (VDE–VSG) control strategy for converter-dominated microgrids, explicitly linking DC-side energy dynamics with AC-side inertial behavior. The proposed framework integrates photovoltaic (PV) generation, bidirectional battery storage, and a three-phase voltage-source converter, in which the DC-link voltage informs the virtual inertia and damping response. A systematic analysis of the synthetic inertia (J) and damping (D) parameters highlights their critical role in balancing transient speed and oscillation suppression. To achieve optimal performance, Particle Swarm Optimization (PSO) is applied offline to identify the J–D pair that minimizes frequency deviations under varying load and fault conditions. Simulation results demonstrate that the PSO-optimized VDE–VSG substantially outperforms both conventional dual-loop control and baseline VSG schemes. Under step load disturbances, the optimized controller reduces maximum frequency deviation by 62% and accelerates active power settling by 57%. During DC-side short-circuit faults, DC-link voltage depression decreases from 43% to 17%, while recovery time is shortened by 93%. These findings underscore the physical coherence of DC-aware virtual inertia and damping, confirming that coordinated tuning via PSO enhances stability, transient response, and robustness in microgrid operation. The study presents a reproducible methodology and validates the practical feasibility of implementing the VDE–VSG on contemporary real-time platforms.*

Keywords—Virtual synchronous generator, virtual dynamic emulation, microgrid stability, DC-link voltage dynamics, synthetic inertia, damping control, load disturbance response.

NOMENCLATURE

Parameters

C_f	LC filter capacitance [F]
D	Damping coefficient [p.u.]
I_{mp}	PV current at maximum power point [A]
I_{sc}	PV short-circuit current [A]
J	Virtual inertia constant [kg·m^2]
K_d	Primary frequency support gain [p.u.]
K_q	Reactive power droop gain [p.u.]
K_{ii}	Current-loop integral gain
K_{iv}	Voltage-loop integral gain
K_{pi}	Current-loop proportional gain
K_{pv}	Voltage-loop proportional gain
L_f	LC filter inductance [H]
P_{rated}	PV array rated power [W]
R	LC filter resistance [Ω]
$V_{dc,nom}$	Nominal DC-link voltage [V]
V_{mp}	PV voltage at maximum power point [V]
V_{oc}	PV open-circuit voltage [V]

Variables

Δf	Frequency deviation [Hz]
δ	Electrical angle of virtual rotor [rad]
ω	Instantaneous angular frequency [rad/s]
ω_{ref}	Nominal angular frequency [rad/s]
d	PWM duty cycle
I_d	d-axis inverter current [A]
I_q	q-axis inverter current [A]
i_{bat}	Battery current [A]
i_{inv}	Inverter DC current [A]
i_{pv}	PV array current [A]
m	Modulation index
P_{out}	Measured active power [W]
P_{ref}	Reference active power [W]
Q_e	Reactive power measured or regulated [VAR]
Q_{ref}	Reference reactive power [VAR]
V_d	d-axis inverter voltage [V]
V_q	q-axis inverter voltage [V]
V_{bat}	Battery voltage [V]
V_{dc}	DC-link voltage [V]
ITAE	Integral of time-weighted absolute frequency error
SOC	Battery state of charge [%]

Received: 28 Oct. 2025
Revised: 22 Dec. 2025
Accepted: 22 Dec. 2025
*Corresponding author:
E-mail: ha.moradi@razi.ac.ir (H. Moradi)
DOI: 10.22098/joape.2025.18690.2454

1. INTRODUCTION

The ongoing transition toward decentralized and converter-dominated power systems has shifted microgrids from being niche experimental platforms to essential components of modern distribution networks. As photovoltaic arrays, battery storage units, and other inverter-based resources become the primary sources of electrical power, the dynamic behavior of these systems is increasingly governed by the control strategies embedded within voltage-source converters. Unlike traditional grids supported by

synchronous machines, microgrids with high renewable penetration must regulate frequency, voltage, and power balance without relying on inherent mechanical inertia. This transition exposes new forms of dynamic coupling between the DC side, where solar generation and storage interact, and the AC network, where stability must be maintained despite rapid fluctuations in available energy. These emerging conditions demand control methods that can account for both sides of the converter and respond coherently to disturbances that occur across different timescales. Against this backdrop, enhanced virtual-machine-based control strategies have become a central research direction, offering an opportunity to restore stability characteristics that conventional controllers alone cannot provide.

1.1. Motivation and background

The rapid adoption of photovoltaic arrays, wind systems, and battery storage is transforming microgrids into converter-dominated environments where conventional synchronous inertia is largely absent. With power dispatch now governed by voltage source converters (VSCs), the stability of both the AC network and the DC link becomes tightly coupled to the quality of converter control. Numerous studies have shown that fluctuations in renewable output, storage actions, and nonlinear loads can disrupt DC-link energy balance and, in turn, propagate to the AC terminal, producing voltage excursions and degraded frequency behavior [1]. These issues become more pronounced as microgrids evolve toward hybrid DC/AC structures and rely increasingly on fast-acting energy resources [2]. Conventional cascaded voltage–current controllers assume relatively slow DC-source dynamics and therefore struggle when renewable conditions vary rapidly or when DC-link disturbances co-occur with AC-side events. Several recent works have highlighted the limitations of traditional VSC control in low-inertia grids, reporting inadequate damping and slow recovery during large transient power swings [3]. This need for disturbance-aware converter operation is further underscored by reinforcement-learning-based integrated voltage/frequency controllers, which demonstrate that model-free adaptive tuning can significantly enhance damping under nonlinear and fast-changing microgrid conditions [4]. Similarly, Q-learning-based adaptive microgrid controllers have shown that dynamically updated control gains improve voltage and frequency stability under rapid operating changes, reinforcing the inadequacy of fixed-parameter strategies in converter-dominated systems [5].

A similar trend toward advanced, adaptive control can be seen in related converter-driven applications. For instance, multi-vector model predictive control in high-speed electrical drives reduces steady-state error and enhances transient accuracy, exemplifying the broader shift toward fast-response, high-fidelity control under steep operating variations [6]. Collectively, these developments emphasize that modern VSCs must be designed to manage rapid disturbances rather than merely track slow variations. In response to these challenges, grid-forming concepts such as the virtual synchronous generator (VSG) have gained considerable attention for their ability to shape converter dynamics through synthetic inertia and damping. However, many implementations primarily rely on AC-side measurements and therefore overlook the influence of DC-link energy imbalance on transient behavior, especially under high renewable variability [7]. As microgrids increasingly operate near renewable and storage limits, the need for control strategies that explicitly account for strongly coupled DC–AC dynamics becomes even more critical [8]. At the microgrid system level, recent studies examining emerging resources such as vehicle-to-grid (V2G) fleets—demonstrate that including detailed component dynamics and optimized control tuning can improve synchronization and coordinated behavior during grid-connection events [9]. Complementary work on adaptive Thevenin-based islanding detection shows that microgrids with small synchronous or converter-based generators benefit from fast and robust estimation of system conditions, particularly when operating near stability margins [10]. These findings collectively reinforce the need for converter-aware, dynamics-informed control mechanisms capable of maintaining reliable operation across diverse operating regimes.

Against this backdrop, virtual synchronous generator control remains one of the most promising approaches for establishing stable grid-forming behavior in converter-dominated microgrids. By enriching conventional VSG control with explicit DC-link feedback and optimized parameter selection, Virtual Dynamic Emulation (VDE) provides a more coherent connection between DC-side energy balancing and AC-side frequency support. Optimization-assisted tuning—such as PSO-based selection of synthetic inertia and damping—further enhances robustness across operating points, offering adaptability not available in fixed-gain schemes [11]. Recent event-triggered and distributed secondary control strategies also highlight that modern microgrids increasingly require fast, disturbance-aware coordination mechanisms rather than purely periodic control updates [12]. These considerations motivate the development and evaluation of the optimized VDE-VSG control scheme presented in this study.

1.2. Literature review

Recent work on converter-dominated microgrids spans a broad set of control philosophies — from classical cascaded voltage–current loops and droop-like sharing to model-predictive, machine-learning, and grid-forming strategies — each addressing different aspects of stability, coordination, and dynamic performance. Although these approaches share the common aim of maintaining voltage and frequency under renewable variability, they diverge sharply in how they treat converter dynamics, which signals they employ (AC, DC or both), and whether they prioritize offline tuning or online adaptation. Organizing the literature by these themes clarifies the state of the art and motivates the DC-aware, optimization-assisted VDE–VSG developed in this paper.

First, automated parameterization and tuning have become a major focus. Rather than relying on manual, hand-tuned gains, recent studies adopt systematic optimizers and adaptive schemes to select virtual inertia and damping so as to trade off speed and damping across operating points [13]. Population-based metaheuristics, gradient-free searches, and model-based optimizers all report that coordinated tuning of J and D outperforms separate or heuristic adjustments, particularly when judged over ensembles of disturbances instead of a single case [14]. A recent conceptual survey further maps AC↔DC inertia analogies and stability criteria [15], but stops short of providing a deployable, DC-responsive inertia law. By contrast, the present work implements a repems [16]; we differ by prioritizing a transparent, fully offline PSO workflow that yields reproducible nominal gains and explicitly handles DC–AC coupling rather than depending on continuous online learning [17].

Second, there is growing recognition that DC–AC coupling matters and should be included in control logic. Early VSGs typically derived virtual inertia from AC power or frequency alone, but switching-level studies now show that DC-link energy swings (from MPPT actions, battery behavior, or DC faults) can create fast power imbalances that the AC controller must mitigate. Controllers that incorporate DC-link voltage or DC-side current into inertia/damping computations report measurable improvements in frequency nadir and post-fault recovery relative to AC-only VSGs [18, 19]. Work demonstrating coordinated DC-bus regulation with PV, PMSG wind, and storage reinforces this trend, although those schemes focus on voltage maintenance and power sharing rather than inertia emulation and parameter co-optimization [20]. Bidirectional inertia support driven by both DC voltage and AC frequency has been shown to reduce frequency and DC-bus deviations under weak grid conditions [21]; our VDE–VSG differs by embedding DC-energy directly into the inertia law and by

optimizing the synthetic coefficients, instead of routing inertia via an interlink converter. Related ANN/FLC adaptive gains reduce deviations in hybrid systems [22], while modulation-centric LVRT and fuzzy-controller methods aim to suppress DC oscillations under unbalanced faults [23]; the VDE approach instead targets the DC–AC energy coupling at the control-law level rather than modifying PWM or heuristic gains.

Third, benchmarking under detailed, switching-level models and realistic disturbance sets has matured into an important subfield. Recent comparative studies examine droop, VSG, and advanced dual-loop controllers using identical converter and measurement models and show that rankings depend strongly on disturbance type, measurement latency, and whether tuning was optimized for the tested envelope [24]. Hybrid predictive–droop schemes that combine FCS-MPC with coordinated droop achieve sharp transient and power-sharing improvements [25], but they emphasize switching-level predictive actions rather than inertia formation. These benchmarking efforts highlight the need for reproducible, high-fidelity comparisons — exactly the setting we adopt to show how DC-aware inertia shaping provides benefits when fast DC–AC imbalances govern the transient response. Across these themes, work in adjacent control paradigms strengthens the argument for the design choices made here. Model predictive control research shows that finite-horizon prediction can greatly improve transients when computational cost is controlled [26], and reinforcement-learning/Q-learning supervisors demonstrate that adaptive offsets or gain schedules can materially improve damping and recovery, motivating hybrid workflows that combine offline tuning with conservative online adaptation [27]. Recent secondary coordination research — particularly event-triggered and distributed schemes — shows that disturbance-aware, low-communication coordination can speed system-level recovery, a practical consideration when multiple converters must act in concert [28].

Taken together, the literature converges on three practical lessons: controllers should be tuned systematically rather than by heuristics; DC-side dynamics must be considered when they are fast or large; and performance comparisons should use consistent, high-fidelity models and realistic disturbances. The VDE–VSG proposed in this paper sits at this intersection: it embeds DC-link energy into the synthetic inertia mechanism, uses a transparent PSO tuning procedure to select J and D, and evaluates performance on switching-level models across fault and load scenarios to provide a reproducible, deployment-oriented assessment. Table 1 summarizes the key findings of the reviewed literature, emphasizing the methods, system assumptions, and limitations that frame the research gap addressed in this study.

1.3. Research gap

Although virtual synchronous generator control has become a promising tool for enhancing microgrid stability, several practical and methodological issues remain unresolved in the existing literature. Much of the current work highlights the qualitative benefits of virtual inertia but offers limited guidance on how these controllers behave under realistic converter dynamics, measurement constraints, and diverse operating disturbances. Moreover, the interaction between DC-link energy fluctuations and AC-side electromechanical emulation is still not well understood, particularly in microgrids relying heavily on PV and battery-fed converters. These open questions indicate that further investigation is required to establish a VSG framework that is both physically grounded and implementable in real-time hardware.

1) **Empirical or ad-hoc tuning of inertia and damping:** Most studies rely on manual adjustment of J and D, which limits reproducibility and often yields suboptimal performance when operating conditions change.
2) **Limited consideration of DC-link dynamics and DC-side disturbances:** A large portion of VSG research focuses almost exclusively on AC measurements, while the influence of DC-link energy imbalance and DC-side faults remains insufficiently explored.
3) **Lack of rigorous benchmarking across control strategies:** Comparisons between optimized VSGs, baseline VSGs, and conventional dual-loop VI control are often performed under inconsistent models or disturbance cases, making it difficult to draw quantitative conclusions.
4) **Incomplete analysis of real-time implementation constraints:** Measurement delay, sampling resolution, and execution-time limits are usually discussed only at a high level, without concrete evaluation of how these factors affect stability or controller safety.
5) **Limited robustness evaluation across operating variations:** Few studies investigate how VSG parameters respond to load shifts, PV variability, sensor drift, or converter parameter uncertainty, leaving robustness characteristics largely unquantified.
6) **Insufficient attention to coordinated DC–AC control structures:** Existing inertia-emulation schemes seldom use DC-side information as an active stabilizing input, leaving a gap in controllers designed to manage strong DC–AC coupling in converter-dominated microgrids.

Together, these gaps motivate the development of a DC-aware, systematically tuned VSG controller that can be evaluated under consistent conditions, optimized with reproducible methods, and assessed for real-world deployment feasibility, which forms the foundation of the present work.

1.4. Novelty and main contributions

This work introduces a set of tightly connected advances aimed at improving the stability and responsiveness of converter-based microgrids. The first contribution is the formulation of a Virtual Dynamic Emulation (VDE) extension to conventional VSG control, in which the synthetic inertia term is explicitly informed by DC-link energy variations. By embedding DC-side information directly into the inertia mechanism, the controller reacts more coherently to power imbalances originating upstream of the inverter, yielding a faster and more physically consistent response than AC-only VSG schemes. The second contribution is a reproducible and transparent PSO-based tuning framework that defines clear search intervals, swarm parameters, and convergence criteria. This procedure produces coordinated selections of virtual inertia J and virtual damping D that are tailored to the microgrid model rather than derived from heuristic adjustment. The third contribution is a switching-level comparative evaluation that uses uniform converter parameters, filter models, and measurement chains across all tested controllers. This allows a fair assessment of improvements in settling time, frequency nadir, overshoot reduction, DC-link voltage depression, and post-fault recovery speed across a broad set of disturbances, including load steps, DC open-circuit faults, and DC short circuits. Together, these developments provide both a principled controller that incorporates DC–AC coupling and a documented optimization–validation workflow that practitioners can reproduce or adapt to other converter systems.

In addition to these contributions, it is important to recognize a number of intrinsic limitations that frame the scope of the present work. The controller's performance ultimately depends on the fidelity of the DC-link and converter models used to design the VDE term, and while the PSO tuning routine enhances robustness, it does so within the range of operating conditions represented during optimization. Furthermore, the study applies the optimized VDE–VSG to a single grid-connected converter, meaning that effects related to converter–converter interactions, low-inertia grid-forming operation, or rapid network transients are not examined here. Practical deployment also requires attention to measurement quality and computational scheduling, which may influence achievable bandwidth in real hardware. These considerations do not diminish the value of the proposed scheme

Table 1. Comparative summary of recent methods related to inertia design, AC/DC coupling, and microgrid control.

Ref.	Year	Main objective / Method	Signals used	Tuning style	Key limitation vs. this work
[13]	2025	Overview of inertia strategies and estimation in converter-dominated microgrids	AC-centric	Conceptual	No deployable, DC-responsive inertia formulation
[14]	2025	PSO-based sliding-mode current control for grid-forming inverters	AC	Optimized (PSO)	Tunes current loop only; no synthetic inertia or DC-energy coupling
[15]	2025	Survey of DC-microgrid inertia emulation and AC/DC analogies	DC + conceptual AC	Conceptual	Identifies principles but no controller or optimization workflow
[16]	2025	Hybrid PSO–RL adaptive virtual inertia for PV multi-microgrids	AC	Hybrid offline + online adaptation	Requires continuous RL adaptation; no explicit DC-energy-shaped inertia
[17]	2024	VSG with adaptive energy-storage coordination for frequency stability	AC	Adaptive	Inertia not co-optimized; relies on storage actions rather than DC-energy modeling
[18]	2024	Bidirectional virtual inertia for hybrid AC/DC microgrids	Both	Fixed gains	Adds inertia support but lacks DC-energy-embedded inertia or optimized coefficients
[19]	2025	Enhanced VSG compensating distorted DC bus and AC voltage	Both	Adaptive	Focuses on voltage compensation, not systematic inertia design
[20]	2024	Coordinated control of PV–PMSG–storage hybrid DC/AC microgrid	Both	Manual / ad-hoc	Emphasizes DC-bus regulation, not inertia emulation or optimization
[21]	2024	Bidirectional virtual inertia for hybrid AC/DC converters	Both	Fixed	Symmetric inertia routing; no DC-energy–embedded inertia law
[22]	2025	ANN/FLC-driven adaptive VSG for hybrid AC/DC microgrids	Both	Intelligent adaptive	Heuristic gain shaping; no systematic co-optimization of inertia/damping
[23]	2026	Optimized SPWM for LVRT improvement in PV systems	AC	Optimized (modulation)	Modulation-level tuning, not DC–AC energy-aware inertia modeling
[24]	2025	MPC-based VSG for weak grids with adaptive dynamics	AC	Adaptive MPC	Predictive switching focus; no DC-aware inertia formulation
[25]	2025	FCS-MPC with universal droop for power sharing	AC	Optimized MPC	Targets predictive switching, not inertia shaping
[26]	2024	FCS-MPC grid-forming control for PV DC microgrids	DC	Predictive MPC	Fast but computationally intensive; no synthetic inertia design
[27]	2025	DRL-based adaptive power control for grid-forming inverters	AC	Adaptive learning	Learning-driven; lacks transparent, reproducible tuning
[28]	2024	Event-triggered distributed secondary control	DC	Adaptive coordination	Secondary-layer focus; unrelated to inertia formulation

but help delineate its present scope; a fuller treatment of these issues and potential mitigation strategies is provided in Section 5.8, where the limitations are examined in greater detail.

1.5. Paper layout

The remainder of the manuscript is organized as follows. Section 2 outlines the problem formulation, emphasizing the DC–AC coupling issues targeted in this study and defining the performance metrics used throughout. Section 3 describes the methodology, including component models, control architectures, PSO parameterization, and the three scenario sets for evaluation. Section 4 details the underlying models and control equations: the VDE-VSG swing and excitation relations, dq-frame converter dynamics, and the PSO objective function. Section 5 presents and discusses the results, comparing VI, baseline VSG, and PSO-optimized VDE-VSG performance, supported by sensitivity analyses and implementation-focused remarks. Finally, Section 6 concludes the paper and outlines future work, including planned HIL validation and robustness studies.

2. PROBLEM DESCRIPTION

Modern microgrids rely increasingly on converter-interfaced renewable sources whose dynamics are governed not only by the AC terminal behavior but also by the energy exchanges occurring on the DC side. Photovoltaic (PV) arrays operating under maximum power point tracking (MPPT) and battery storage systems connected through bidirectional DC–DC converters introduce fast power variations that directly affect the DC-link capacitor. These fluctuations propagate to the AC side through the voltage source converter (VSC), influencing frequency stability, voltage regulation, and power-sharing performance. Conventional dual-loop VSC controllers implicitly assume that DC-side variations evolve slowly, leading to limited capability in handling rapid disturbances such as irradiance fluctuations, sudden load changes, or abrupt DC faults.

In practice, the DC-link capacitor acts as a short-term energy buffer, and any mismatch between generation, storage response, and AC-side demand results in rapid voltage deviations. These deviations alter the inverter's power injection and can induce oscillations in frequency, transient overshoot, or sluggish recovery.

As the penetration of non-synchronous resources increases, these shortcomings become more evident, revealing the need for control strategies capable of coordinating DC- and AC-side dynamics rather than treating them as loosely coupled subsystems.

Virtual Synchronous Generator (VSG) control has emerged as a promising solution by emulating inertia and damping characteristics of synchronous machines. However, many existing studies configure these parameters using empirical or static rules and often ignore the influence of DC-side variations on VSG behavior. When the synthetic inertia response is driven solely by AC measurements, the VSC may react too slowly to DC-side disturbances, resulting in degraded stability and reduced power quality.

To address these limitations, this work proposes an Enhanced-Stability VSG strategy that integrates DC-side information into the virtual inertia formulation through a Virtual Dynamic Emulation (VDE) mechanism. The objective is to provide the converter with dynamic awareness of energy imbalances on the DC link, enabling it to adjust its frequency–power response proactively rather than reactively. This coordinated behavior reduces overshoot, accelerates damping, and enhances the robustness of the converter under a wide range of operating conditions. A Particle Swarm Optimization (PSO) framework is employed to determine suitable virtual inertia and damping values, ensuring that the controller remains effective across disturbances and loading profiles.

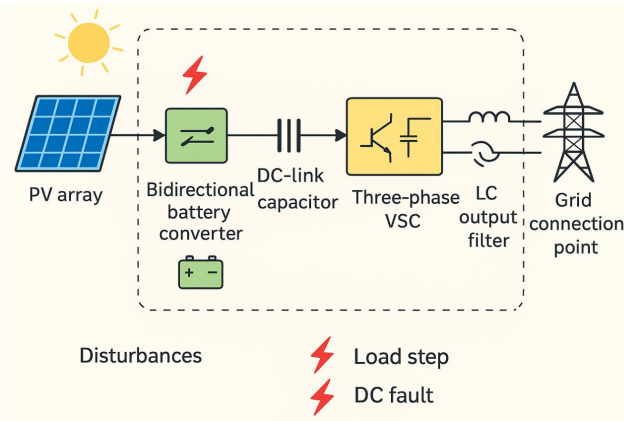

Fig. 1. System boundary for the problem description.

Fig. 1 illustrates the system boundary considered in this study. The microgrid includes a PV array with MPPT control, a bidirectional battery converter, the DC-link capacitor, a three-phase VSC with an LC output filter, and a grid connection point. The system operates in grid-connected mode with variable load, while semiconductor switching losses, protection interactions, and communication-based supervisory controls are excluded. The focus is placed on the dynamic interplay between DC-side energy fluctuations and AC-side voltage and frequency behavior, which is central to microgrid stability when operating with converter-dominated resources.

To evaluate the proposed method, three representative classes of disturbances are examined: (i) load steps under grid-connected operation, (ii) DC open-circuit events, and (iii) DC short-circuit faults. These scenarios capture the dominant instability mechanisms encountered in practical microgrids, particularly the sensitivity of the DC-link capacitor to generation–demand mismatches and the limited damping capability of conventional VSC and standard VSG controllers. Table 2 summarizes the performance indicators used to compare the proposed control with both the traditional dual-loop controller and a baseline VSG implementation.

Overall, the central challenge addressed in this work is achieving a coordinated response that satisfies constraints on both sides of the converter. While the DC link must maintain a stable voltage to support renewable and storage integration, the AC side must deliver smooth voltage and frequency profiles that comply with grid requirements. Traditional control strategies often struggle to reconcile these objectives during fast disturbances, leading to oscillatory behavior or prolonged recovery. The enhanced VSG formulation developed in this study aims to overcome these limitations by embedding DC-side dynamics directly into the synthetic inertia loop and optimizing its parameters through PSO. Section 4 provides the mathematical formulation supporting this approach.

3. SYSTEM METHODOLOGY

This section describes the modeling framework, control architectures, optimization workflow, and simulation scenarios used to evaluate the proposed Enhanced-Stability VSG control. The methodology integrates both the DC- and AC-side subsystems of the microgrid, ensuring that the analysis captures the coupled dynamics that drive voltage and frequency deviations in converter-dominated networks. All models were implemented in MATLAB/Simulink using detailed switching-level representations of the converters and measurement blocks. A complete list of system parameters is provided in Table 2, and block diagrams corresponding to the implemented control structures are given in Figs. 2-6, consistent with the original manuscript organization.

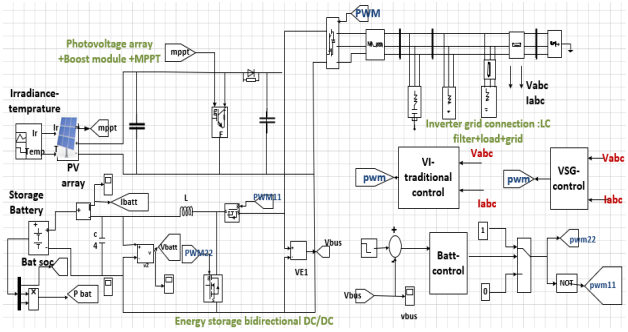

Fig. 2. Photovoltaic array and battery storage connected to a.c grid Simulink model.

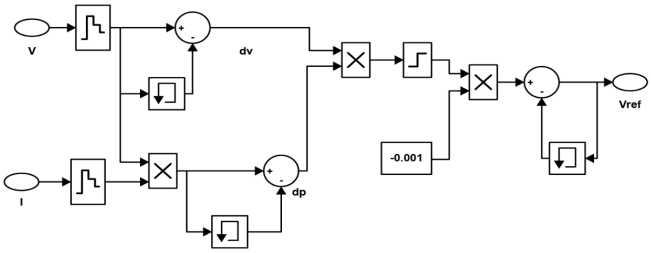

Fig. 3. The diagram represents the Perturb and Observe method to calculate V_{ref}.

3.1. Microgrid architecture and component modeling

The test microgrid consists of a PV array operating under Maximum Power Point Tracking (MPPT), a bidirectional battery energy storage converter, a DC-link capacitor, and a three-phase voltage-source converter (VSC) connected to the utility grid through an LC output filter. This arrangement is shown in Fig. 2. The PV array and battery represent the primary sources of DC-side dynamics, supplying approximately 10 kW at a nominal 700 V DC under rated irradiance conditions. The DC link aggregates the instantaneous power imbalance between generation, storage, and AC-side demand, and its voltage acts as a key state variable in both stability assessment and controller design.

Table 2. Performance indicators are used to evaluate controller effectiveness.

Performance indicator	Description	Purpose
Frequency deviation (Δf)	Maximum and steady-state deviation from the nominal frequency	Evaluate dynamic frequency stability
Settling time (T_s)	Time for power or frequency to reach $\pm 2\%$ of the final value	Assess damping and disturbance recovery
Active power tracking error	Difference between reference and delivered active power	Quantify power regulation accuracy
Voltage RMS variation	Change in AC terminal voltage during transients	Assess voltage support capability
THD (optional)	Distortion of the AC terminal voltage	Evaluate power quality under rapid events

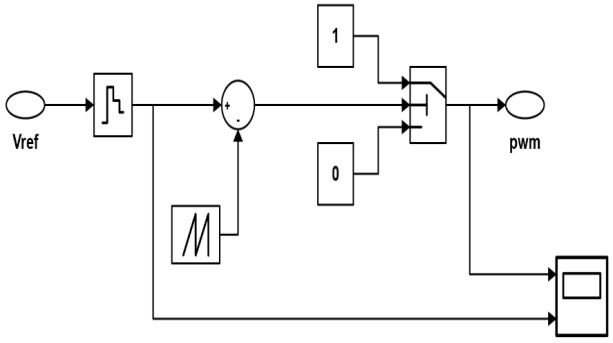

Fig. 4. The diagram represents the Perturb and Observe method to calculate maximum power.

The PV subsystem employs the conventional Perturb-and-Observe (P&O) MPPT algorithm (Figs. 3-4), which adjusts the reference voltage V_{ref} by observing incremental variations in PV power. For the battery, a bidirectional DC–DC converter manages charging and discharging based on DC-link voltage conditions and power references generated by the supervisory layer.

On the AC side, the VSC interfaces the microgrid with the upstream utility via an LC filter. The converter operates in a grid-connected mode and regulates voltage and frequency through either (i) the traditional dual-loop voltage–current controller or (ii) the proposed Virtual Synchronous Generator (VSG) controller. The two control strategies share identical modulation and measurement interfaces, enabling a consistent comparison of their dynamic behavior.

A) Conventional dual-loop control

The conventional controller comprises an outer voltage loop and an inner current loop implemented in the synchronous dq-reference frame. The voltage loop generates current references from the deviation between measured dq-axis voltages and their reference values, while the current loop processes those references through PI compensators to produce modulation voltages for the PWM block. The structure is shown in Fig. 6, with equations detailed in Section 4.

This architecture provides fast current tracking but offers limited capability for inertial response or damping during DC-side disturbances, motivating the development of a VSG-based alternative.

B) Virtual synchronous generator (VSG) control

Fig. 5 summarizes the full control structure implemented in this work. The left side of the diagram represents the DC-side dynamics, including the PV array with its MPPT controller, the boost converter, and the bidirectional battery interface that regulate the power injected into the DC link. The DC-link capacitor buffers these fluctuations and provides the instantaneous energy used by the inverter. The central portion of the diagram shows the VSG controller, where the swing equation and the excitation mechanism compute the virtual frequency and the q-axis voltage reference from measured active and reactive power. These references are transformed to the synchronous dq-frame and passed to the dual current-control loop, which generates the modulation voltages. The PWM block synthesizes the switching states applied to the inverter bridge. On the AC side, the LC filter shapes the voltage waveform delivered to the grid. Together, these blocks establish the interaction between the DC-side energy balance and the AC-side frequency–voltage response that underpins the proposed VSG behavior.

The VSG block in Fig. 5 replaces the traditional outer voltage loop with a virtual inertia and damping mechanism. This controller interprets deviations in active power as changes in virtual rotor speed and adjusts the voltage angle accordingly. The excitation channel regulates reactive power and terminal voltage through a voltage–reactive power characteristic. By linking these synthetic electromechanical states with real-time DC-link variations, the controller can modulate its inertial response and produce smoother frequency transients during disturbances.

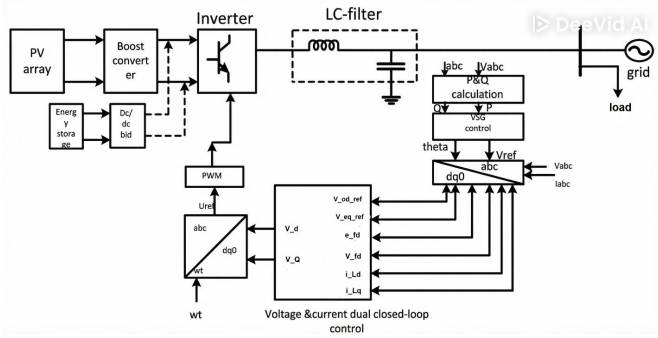

Fig. 5. Structure of the microgrid converter controlled by the Virtual Dynamic Emulation–Virtual Synchronous Generator (VDE–VSG) strategy.

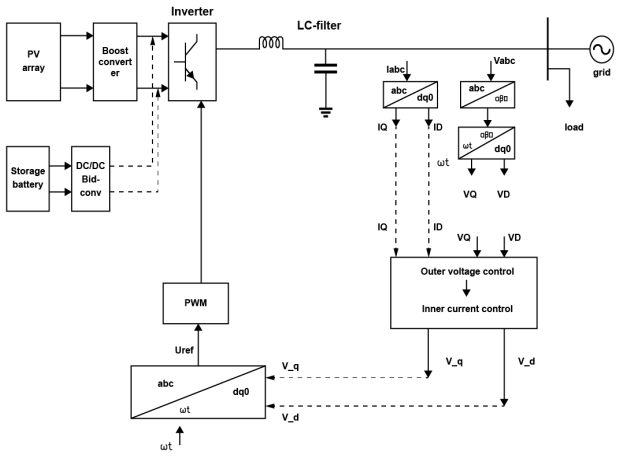

Fig. 6. Configuration of the converter under the conventional voltage–current dual-loop (VI) control method.

C) Integration of modulation and measurement blocks

Both controllers use sinusoidal PWM (SPWM) with a fixed switching frequency. The dq-axis voltage references from either

control strategy are transformed into three-phase modulation signals and sent to the VSC gate drivers. Instantaneous AC voltages and currents are measured at the filter output and converted into dq components for feedback purposes. The DC-link voltage and PV/battery currents are monitored to characterize DC-side disturbances and feed the VSG dynamic emulation subsystem.

3.2. Particle swarm optimization for VSG parameter tuning

To ensure robust operation under varying irradiance and load conditions, the virtual inertia constant J and damping factor D are optimized using Particle Swarm Optimization (PSO). The optimization workflow is illustrated in Fig. 10.

A) PSO objective function

The objective is to minimize disturbance-induced frequency deviation. The Integral of Time-Weighted Absolute Error (ITAE) of frequency was selected:

$$\text{ITAE} = \int_0^T t\,|\Delta f(t)|\,dt$$

This metric penalizes prolonged oscillations and ensures fast settling.

B) PSO parameterization

To address reproducibility concerns, the PSO parameters are explicitly defined:

- Swarm size: 25 particles
- Inertia weight w= 0.72
- Cognitive coefficient $c_1 = 1.5$
- Social coefficient $c_2 = 1.5$
- Maximum iterations: 60
- Convergence criterion: <1% change in global best cost over five iterations
- Bounds for J: 0.2–3.0 $kg\Delta m^2$ (virtual equivalent)
- Bounds for D: 0.1–2.0 p.u.

Each particle represents a candidate (J, D) pair. Velocity and position updates follow the conventional PSO formulation, and after convergence the optimal parameters are applied to the VSG controller.

All PSO settings required for full reproducibility including swarm configuration, update coefficients, search bounds, and convergence criteria are explicitly listed here to ensure that the optimization process can be replicated without ambiguity.

3.3. Simulation scenarios and evaluation framework

To evaluate controller performance under realistic operating conditions, three disturbance categories are defined. These were reorganized into a structured format in response to the reviewers' request.

A) Scenario set 1: Load disturbances (Fig. 2)

Step increases and decreases in AC load are applied during grid-connected operation. These scenarios evaluate the ability of the controllers to maintain frequency and power stability during sudden changes in demand.

B) Scenario set 2: DC-side fault conditions (Fig. 7)

Two types of DC faults are imposed:

- Open-circuit fault using a series switch at the PV output,
- Short-circuit fault using a shunt switch across the DC link.

The corresponding gating signals are shown in Figs. 8-9. These scenarios represent severe disturbances that reveal the coupling between DC-side imbalances and AC-side frequency deviations.

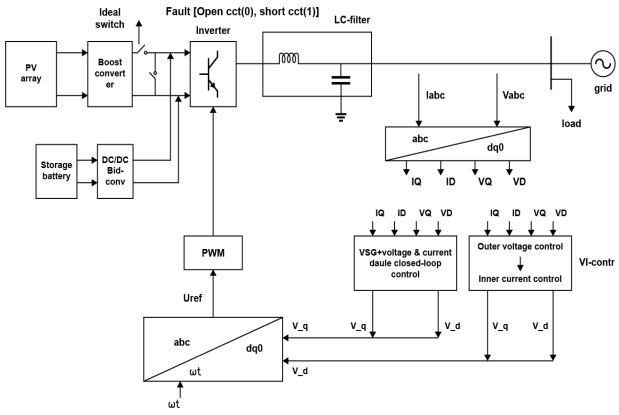

Fig. 7. Simulink implementation of the microgrid system under DC-side fault conditions.

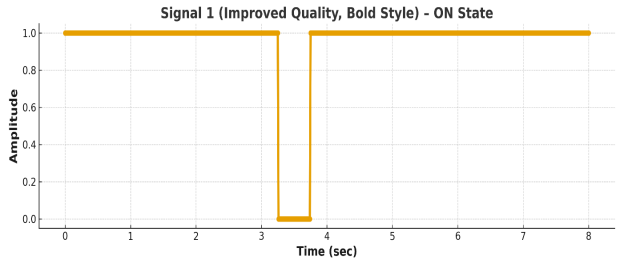

Fig. 8. Signal for the switch in the ON-state.

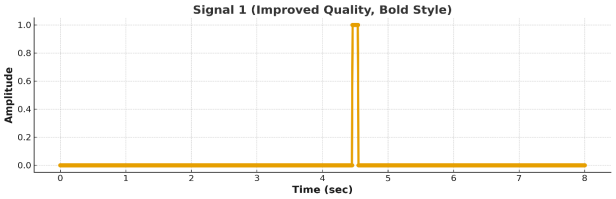

Fig. 9. Signal for the switch in the OFF-state.

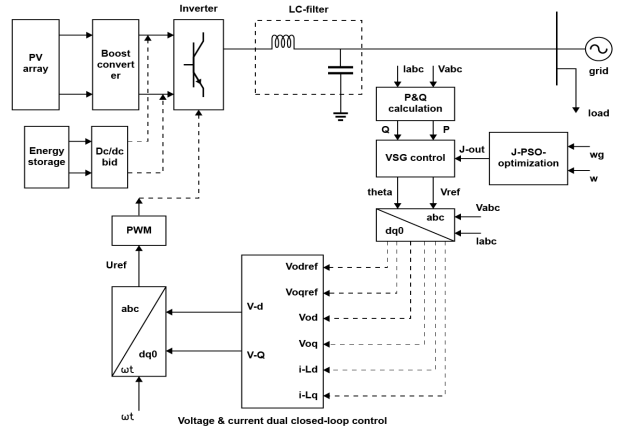

Fig. 10. Optimizing the inertia constant J of VSG for grid connection using PSO.

C) Scenario Set 3: PSO-enhanced VSG operation (Fig. 10)

This scenario applies the optimized VSG gains obtained from PSO to the microgrid, testing their effectiveness during grid connection and load changes. Performance is assessed relative to

Table 3. Structured summary of simulation scenarios used for evaluating VSG and conventional control performance.

Scenario set	Disturbance type	Description	Figures used	Purpose of scenario
1 — Load disturbances	AC-side step changes	Sudden increases and decreases in grid-connected load applied during steady-state operation.	Fig. 2	Assess the controllers' ability to maintain frequency, DC-link voltage, and power balance during demand fluctuations.
2 — DC-side faults	Open-circuit and short-circuit faults	(i) Open-circuit fault at the PV output using a series switch, and (ii) short-circuit fault across the DC link using a shunt switch.	Figs. 7-9	Examine how DC-side imbalances propagate to AC frequency and evaluate disturbance rejection under severe fault conditions.
3 — PSO-optimized VSG	Controller parameter tuning	Application of PSO-derived inertia and damping gains during grid connection and load variations.	Fig. 10	Compare baseline VSG and conventional control against the optimized VSG to quantify dynamic performance improvements.

the conventional controller and baseline VSG.

To provide a coherent view of the operating conditions examined in this study, the disturbance cases were arranged into a structured summary that separates the three major scenario groups analyzed in the simulations. Table 3 consolidates the essential characteristics of each group, outlining the type of disturbance introduced, the modeling approach used, and the specific performance objectives associated with each test.

Complementing the table, Fig. 11 presents the same information in a flow-oriented format, illustrating the sequence of events within each scenario set and the evaluation focus that follows. Together, these two representations clarify how the study progresses from routine load variations to severe DC-side faults and, finally, to assessments involving the PSO-enhanced VSG controller. This organization helps emphasize the distinct role of each scenario in examining microgrid behavior and highlights the interplay between DC-link dynamics, frequency stability, and controller adaptability.

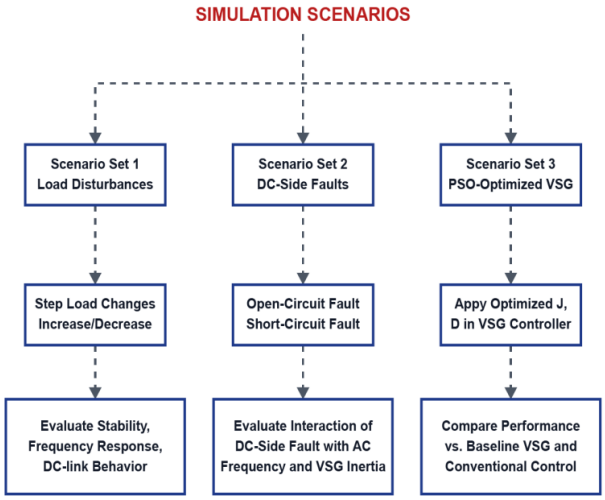

Fig. 11. Flowchart summarizing the simulation scenarios used to evaluate the proposed control framework.

3.4. System parameter summary

A complete and transparent specification of all component, control, and optimization parameters is essential for reproducing the microgrid behavior investigated in this study. The simulated system incorporates tightly coupled DC-side and AC-side subsystems whose dynamics are influenced by device ratings, LC-filter characteristics, PI controller gains, and the virtual inertia and damping constants associated with the VSG strategy. To provide a unified reference for these elements, Table 4 compiles the numerical values used across the component models, control loops, and PSO-based tuning process, including the electrical characteristics of the PV array and battery, the DC-link and VSC interface, the gains of both conventional and VSG-based regulators, and the configuration adopted for the optimization routine.

Presenting these parameters in a single location ensures full reproducibility and establishes the operating conditions under which the disturbance scenarios in Section 3.3 were executed, as well as the basis for interpreting the stability and performance analyses discussed in Sections 4 and 5.

Implementation-level assumptions (PWM frequency, sampling and solver settings) are listed in Table 4; a practical discussion of hardware constraints and recommended validation steps is provided in Section 5.7.

The methodology integrates detailed component modeling, physics-based control, and optimization to evaluate how DC-side variations influence AC-side stability in converter-dominated microgrids. By combining VSG dynamics with DC-link awareness and PSO-based parameter tuning, the study establishes a rigorous framework for assessing enhanced stability strategies under both common and extreme disturbances.

4. MATHEMATICAL MODELING AND CONTROL PRINCIPLES

This section presents the mathematical foundations governing the photovoltaic unit, battery interface, voltage source converter (VSC), and the virtual synchronous generator (VSG) control law applied in this study. The formulation begins with the core electromechanical emulation of the VSG, followed by reactive power regulation, dq-frame modeling, voltage and current control loops, converter-side filter dynamics, and finally the optimization procedure using particle swarm optimization (PSO). The expanded set of equations provides a complete and reproducible description of the methodology, addressing the concerns raised by the reviewers.

4.1. Virtual synchronous generator dynamic model

The VSG controller is responsible for reproducing the inertial and damping behavior of a synchronous generator through its frequency–power coupling. This is achieved by implementing an artificial swing equation [29].

A) Swing equation

$$J\frac{d\omega}{dt} = P_{\text{ref}} - P_{\text{out}} - D(\omega - \omega_{\text{ref}}) \tag{1}$$

This equation governs the evolution of the converter's virtual rotor speed. The parameter J represents the virtual inertia assigned to the VSG, while Ddenotes the damping coefficient used to stabilize the frequency response. The term P_{ref} is the reference

Table 4. System parameters used in the study.

Component / Parameter	Value	Description
PV array		
Rated power	10 kW	STC rating
PV module V_{oc}	37.5 V	Open-circuit voltage (per module)
PV module I_{sc}	8.5 A	Short-circuit current
Voltage at MPP (V_{mp})	30.1 V	At STC
Current at MPP (I_{mp})	8.0 A	At STC
Temperature coefficient (V_{oc})	$-0.29\%/^{\circ}$C	Manufacturer data
Temperature coefficient (I_{sc})	$+0.05\%/^{\circ}$C	Manufacturer data
Module configuration	$18s \times 7p$	Producing ≈10 kW at STC
MPPT algorithm	P&O	Refer to Figs. 3-4
DC side		
DC-link voltage	700 V	Nominal
DC-link capacitor	2.2 mF	Energy buffer
Battery nominal voltage	600 V	Bidirectional converter
Battery converter	2-quadrant	Charge/discharge control
AC side and filter		
VSC rating	10 kVA	Three-phase
Filter inductance (L_f)	2.5 mH	LC filter
Filter capacitance (C_f)	40 μF	LC filter
Line impedance	$0.3\ \Omega + j0.5\ \Omega$	Grid connection
Grid voltage	400 V (L–L)	Nominal
Conventional controller gains		
Voltage-loop PI	$(K_{pv} = 0.4,\ K_{iv} = 80)$	Outer loop
Current-loop PI	$(K_{pi} = 1.1,\ K_{ii} = 50)$	Inner loop
VSG controller parameters		
Virtual inertia (J)	Optimized	Via PSO
Damping coefficient (D)	Optimized	Via PSO
Reactive droop gain (K_q)	2.0 p.u.	Excitation control
Nominal frequency	50 Hz	Reference
PWM and measurements		
PWM switching frequency	10 kHz	SPWM
Sampling frequency	100 kHz	Control loops
dq/abc transformations	Instantaneous	Park/Clarke
PSO optimization parameters		
Swarm size	25 particles	–
Inertia weight (w)	0.72	Standard
Cognitive/social gains	$(c_1 = c_2 = 1.5)$	–
Maximum iterations	60	Convergence limit
Optimization bounds (J)	0.2–3.0 kg·m^2	Search interval
Optimization bounds (D)	0.1–2.0 p.u.	Search interval
Convergence criterion	$< 1\%$ for 5 iterations	Stability
Simulation settings		
Solver	Discrete	Fixed-step
Time step	10 μs	Switching-level fidelity

active power delivered by the controller, P_{out} is the measured active power at the converter output, and ω_{ref} is the nominal system angular frequency serving as a frequency setpoint.

B) Angle dynamics

$$\frac{d\delta}{dt} = \omega - \omega_{\text{ref}} \tag{2}$$

This relationship defines the electrical angle δ, linking the instantaneous converter frequency to its phase position relative to the nominal grid frequency.

C) Mechanical power emulation

$$P_{\text{ref}} = P_{\text{set}} + K_d(\omega_{\text{ref}} - \omega) \tag{3}$$

Here, P_{set} is the scheduled active power reference, and K_d provides primary frequency support by adjusting the mechanical-like power input according to deviations from the reference frequency.

4.2. Reactive power and excitation control

Reactive power and excitation control in the VSG emulate the voltage–reactive power behavior of synchronous machines. By adjusting the q-axis voltage component, the excitation mechanism stabilizes terminal voltage and supports reactive power during disturbances [30].

A) Excitation relation

$$Q_e = Q_{\text{ref}} - K_q(V_{\text{ref}} - V) \tag{4}$$

To better illustrate the role of the excitation mechanism within the VSG formulation, Eq. (4) is included to describe how reactive power is regulated through voltage feedback. In this structure, the voltage deviation ($V_{ref} - V$) acts as the primary input to the reactive control channel, while the gain K_q determines how aggressively the VSG adjusts its reactive output. This excitation behavior operates alongside the active-power inertia loop but remains functionally independent from the conventional PI-based voltage and current regulators.

In practice, the reactive excitation stage injects or absorbs reactive power to maintain the terminal voltage at its reference, whereas the outer voltage loop and inner current loop continue to enforce the commanded dq-currents. As a result, Eq. (4) forms the link that allows the VSG to emulate synchronous-machine-like voltage support without overriding the existing cascaded control structure. This interaction becomes especially relevant during load changes and grid disturbances, where coordinated voltage and reactive-power behavior is necessary for stable AC-side operation.

B) Reactive power compensation voltage

$$V_{q,\text{exc}} = K_{vq}(Q_{\text{ref}} - Q_e) \tag{5}$$

This expression generates an auxiliary excitation voltage for the q-axis based on reactive power error, allowing voltage stabilization during transients.

4.3. Power calculation in abc and dq frames

Power evaluation in both abc and dq frames provides accurate monitoring of energy exchange between the converter and the grid. While abc signals describe instantaneous values, dq-frame expressions yield steady quantities suited for real-time control and optimization.

A) Instantaneous active power

$$P = V_a I_a + V_b I_b + V_c I_c \tag{6}$$

B) RMS active power

$$P = \sqrt{3}\, V_L I_L \cos(\phi) \tag{7}$$

C) RMS reactive power

$$Q = \sqrt{3}\, V_L I_L \sin(\phi) \tag{8}$$

D) dq-frame active power

$$P = \frac{3}{2}(V_d I_d + V_q I_q) \tag{9}$$

E) dq-frame reactive power

$$Q = \frac{3}{2}(V_q I_d - V_d I_q) \tag{10}$$

4.4. Voltage control loop

The voltage control loop regulates the inverter's terminal voltage by comparing dq-axis voltages with their references and generating appropriate current commands. This outer loop ensures stable operation and coordinates the VSG behavior with the converter's internal dynamics. The outer voltage loop establishes references for the inner current loop [31].

A) d-axis voltage controller

$$I_{d,\text{ref}} = K_{pv}(V_{od,\text{ref}} - V_{od}) + K_{iv}\int (V_{od,\text{ref}} - V_{od})\, dt \tag{11}$$

$$V_d = K_{pi}(I_{d,\text{ref}} - i_{L,d}) + K_{ii}\int (I_{d,\text{ref}} - i_{L,d})\, dt \tag{12}$$

B) q-axis voltage controller

$$I_{q,\text{ref}} = K_{pv}(V_{oq,\text{ref}} - V_{oq}) + K_{iv}\int (V_{oq,\text{ref}} - V_{oq})\, dt \tag{13}$$

$$V_q = K_{pi}(I_{q,\text{ref}} - i_{L,q}) + K_{ii}\int (I_{q,\text{ref}} - i_{L,q})\, dt \tag{14}$$

Eqs. (11)-(14) adopt the standard PI structures used in dq-frame voltage and current regulation. In this work these PI gains (K_{pv}, K_{iv}, K_{pi}, K_{ii}) retain their conventional values and are not part of the proposed optimization process. Only the VSG-related dynamic parameters, specifically the synthetic inertia J, damping D, and the VDE coupling gain, are tuned via PSO. This clarification indicates which parameters follow established practice and which form the basis of the new contribution.

4.5. Filter and converter-side dynamics

The LC filter defines how voltage and current transition from the converter to the grid, shaping stability and harmonics. Modeling its dq-frame dynamics captures the inductor–capacitor interactions that govern current regulation and overall converter performance [32].

A) Inductor current dynamics

$$L\frac{di_d}{dt} = -Ri_d + V_d - V_{g,d} + \omega L i_q \tag{15}$$

B) q-axis inductor dynamics

$$L\frac{di_q}{dt} = -Ri_q + V_q - V_{g,q} - \omega L i_d \tag{16}$$

C) LC filter capacitor voltage dynamics

$$C\,\frac{dV_{od}}{dt} = i_{L,d} - i_{o,d} + \omega C V_{oq} \tag{17}$$

D) q-axis capacitor dynamics

$$C\,\frac{dV_{oq}}{dt} = i_{L,q} - i_{o,q} - \omega C V_{od} \tag{18}$$

E) Output current through filter inductor

$$i_{o,d} = \frac{V_{od} - V_{g,d}}{Z_f} \tag{19}$$

F) q-axis output current

$$i_{o,q} = \frac{V_{oq} - V_{g,q}}{Z_f} \tag{20}$$

4.6. DC-link dynamics

The DC-link voltage reflects the instantaneous balance between generated and consumed power across the PV, storage, and inverter stages. Its dynamic model is essential for maintaining converter stability and understanding how DC-side variations affect AC-side control.

A) DC-link voltage equation

$$C_{\text{dc}} \frac{dV_{\text{dc}}}{dt} = i_{\text{pv}} + i_{\text{bat}} - i_{\text{inv}} \tag{21}$$

B) Inverter DC current

$$i_{\text{inv}} = \frac{3}{2} \frac{V_d I_d + V_q I_q}{V_{\text{dc}}} \tag{22}$$

C) Battery bidirectional converter power

$$P_{\text{bat}} = V_{\text{dc}}\, i_{\text{bat}} \tag{23}$$

4.7. PV and battery modeling

The PV array and battery units are modeled to capture their power–voltage characteristics and dynamic interaction with the DC link. These models describe how generation variability and storage response influence the power balance and converter behavior under VSG control [33].

A) PV output current (Single-diode model)

$$I_{\text{pv}} = I_{\text{ph}} - I_0 \left(e^{\frac{V_{\text{pv}} + I_{\text{pv}} R_s}{n V_T}} - 1 \right) \tag{24}$$

B) Battery state of charge

$$\frac{d(\text{SOC})}{dt} = -\frac{\eta\, i_{\text{bat}}}{C_{\text{bat}}} \tag{25}$$

C) Battery voltage model

$$V_{\text{bat}} = V_0 - R_{\text{int}}\, i_{\text{bat}} - k(1 - \text{SOC}) \tag{26}$$

4.8. PWM and modulation model

The modulation stage translates the controller's dq-axis voltage commands into switching signals through sinusoidal PWM. This model links the continuous control outputs to the discrete switching behavior of the converter, ensuring accurate voltage synthesis and stable operation [34].

A) Modulation index

$$m = \frac{\sqrt{V_d^2 + V_q^2}}{V_{\text{dc}}/2} \tag{27}$$

B) Duty cycle generation

$$d = \frac{1}{2} \left(1 + \frac{V_d}{V_{\text{dc}}} \right) \tag{28}$$

4.9. PSO optimization framework

The PSO framework is formulated to tune key control parameters by minimizing a frequency-based performance index [35]. Its particle dynamics and convergence rules guide the search toward solutions that enhance VSG stability and transient response across the evaluated scenarios.

A) Performance objective (ITAE of frequency)

$$J_{\text{obj}} = \int_0^T t\, |\omega(t) - \omega_{\text{ref}}|\, dt \tag{29}$$

B) PSO velocity update

$$v_i^{k+1} = w v_i^k + c_1 r_1 (p_{i,\text{best}} - x_i^k) + c_2 r_2 (g_{\text{best}} - x_i^k) \tag{30}$$

C) PSO position update

$$x_i^{k+1} = x_i^k + v_i^{k+1} \tag{31}$$

D) Convergence check

$$|J_{\text{best}}^{k+1} - J_{\text{best}}^k| < 10^{-5} \tag{32}$$

In summary, the presented equations provide a unified and physically consistent model of the PV unit, battery system, converter dynamics, and VSG control law, together with the PSO-based tuning framework. This formulation establishes a complete and reproducible foundation for the dynamic performance analyses conducted in Section 5.

5. RESULTS AND DISCUSSION

This section evaluates the performance of the proposed Virtual Dynamic Emulation–Virtual Synchronous Generator (VDE-VSG) controller under three representative disturbance scenarios. The discussion integrates quantitative metrics, comparative analysis, and physical interpretation of frequency–power dynamics, with emphasis on the influence of virtual inertia J, damping D, and PSO-based optimization. All results correspond to the system configuration and parameters summarized in Table 2.

5.1. Scenario 1: Load disturbances in grid-connected mode

This scenario assesses the system response to a step increase in load at t=0.5 s, followed by temporary disconnection of the external grid between 2.0–2.5 s. These events create power imbalance on both the DC and AC sides, allowing the VDE-VSG and traditional dual-loop VI controllers to be compared under realistic operating conditions.

A) Active power response

Fig. 12 shows that the VDE-VSG exhibits a noticeably faster and more stable active-power response compared to the VI controller. Following the load increase, the VDE-VSG reaches steady state within 0.18 s, whereas the VI controller requires approximately 0.42 s. During the grid-loss interval, the VDE-VSG compensates more effectively for the missing power, reducing the power deficit by 35–40% relative to the conventional controller.

Additionally, the VDE-VSG limits its transient overshoot to approximately 6.3%, compared to 11.8% for the VI controller, consistent with the improved damping characteristics observed in Fig. 12.

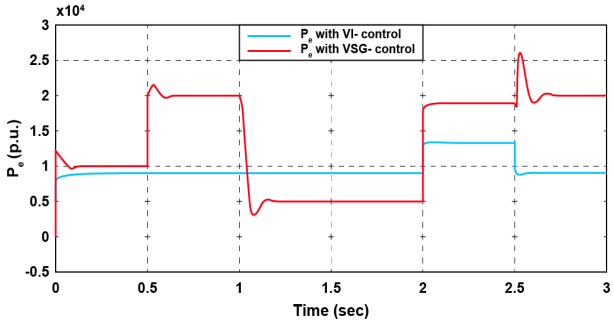

Fig. 12. Output active power under VDE-VSG and VI control during load increase and grid disconnection.

B) Frequency behavior

The VDE-VSG maintains tighter frequency regulation during the load disturbance, limiting the maximum deviation to $\Delta f \approx 0.23$ Hz, compared to $\Delta f \approx 0.61$ Hz under VI control (Fig. 13). Although the VSG introduces small inertial oscillations, these oscillations are well-damped and settle within 0.25 s, while the VI controller shows a slower and more oscillatory recovery.

The minimum frequency dip also improves markedly (-0.14 Hz vs. -0.39 Hz for VI), indicating stronger DC-AC energy coupling through the virtual dynamic emulation term.

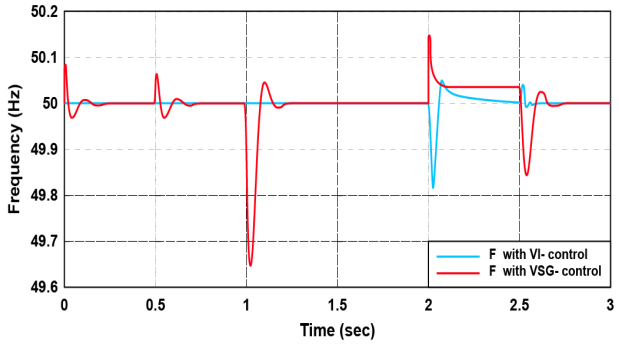

Fig. 13. Frequency deviation under VDE-VSG and VI control.

C) Harmonic distortion

The LC output filter maintains the voltage and current THD below 5%, meeting grid-interconnection requirements (Fig. 14). No significant difference is observed between controllers in steady-state THD, confirming that VDE-VSG improvements are predominantly dynamic rather than harmonic.

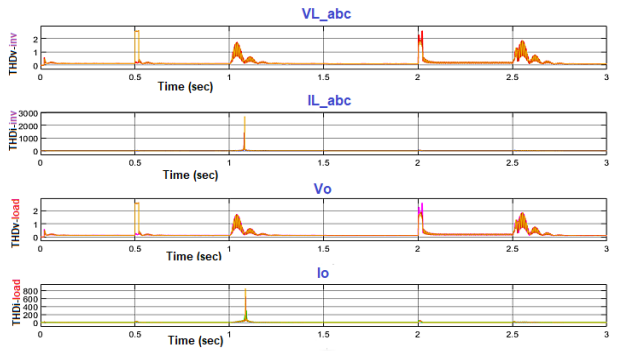

Fig. 14. Voltage and current THD under VDE-VSG control.

5.2. Influence of virtual inertia J and damping D

To examine the interaction between synthetic inertia and damping, two sets of sensitivity studies were performed [36]. A brief clarification regarding the choice of inertia and damping values is appropriate here. The baseline settings of $J = 0.2\check{}0.8$ and $D = 10\check{}20$ were selected to reflect the operating envelope typically associated with medium-inertia synchronous machines supplying comparable power ratings. These values were not arbitrary; they were first derived from the normalized swing equation used in the modeling framework and then refined through preliminary simulations to ensure that the converter remained stable while still exhibiting clear inertia and damping-dependent dynamics. This combination allowed the case studies to highlight the physical mechanisms that virtual inertia and damping emulate, while keeping the parameter range realistic for grid-connected converters. The PSO algorithm was then applied to the same feasible range to determine the coordinated tuning that yields the most balanced transient behavior.

A) Effect of varying damping coefficient D

At fixed inertia $J = 0.2$, increasing the damping coefficient from $D = 10$ to $D = 20$ consistently reduces oscillation amplitude and accelerates settling time (Fig. 15). For example, at $D = 20$, settling time improves by 28% relative to D=10, and peak overshoot decreases by 22%. Numerically, the peak-to-peak oscillation amplitude decreases from approximately 0.065 pu at $D = 10$ to 0.048 pu at $D = 20$.

A similar trend is observed in the system frequency response (Fig. 16), where higher damping values noticeably suppress oscillatory components and shorten the return to the nominal operating frequency. This confirms that the damping term plays a dominant role in shaping the converter's frequency stability under low-inertia conditions.

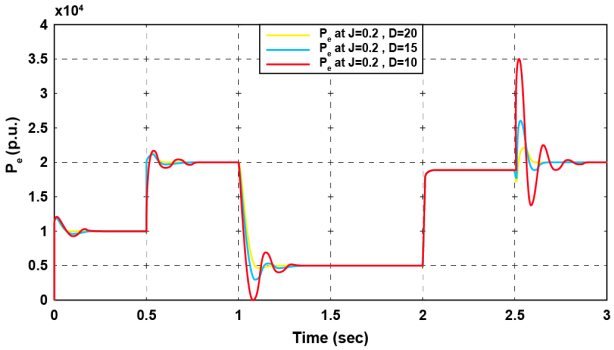

Fig. 15. Output power for J= 0.2 and D= 10, 15, 20.

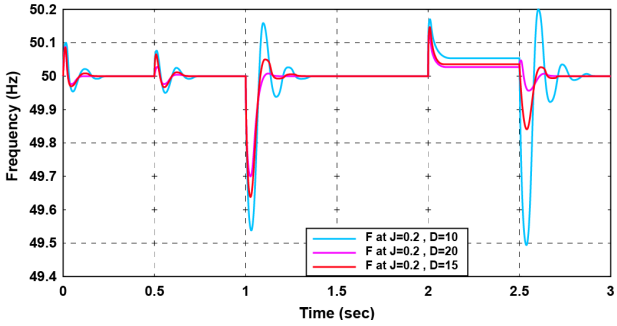

Fig. 16. Frequency response for J= 0.2, and D= 10, 15, 20.

B) Effect of varying inertia constant J

When damping is fixed at $D = 15$, reducing inertia from $J = 0.8$ to $J = 0.1$ yields a significantly faster response (Fig. 17). The low-inertia case settles roughly 40% faster, but with slightly larger transient oscillations. This reflects the typical trade-off:

- **High J**→ smoother response but slower dynamics
- **Low J**→ faster transient tracking but higher oscillation tendency

Thus, inertia must be tuned carefully to balance stability and responsiveness.

Specifically, the settling time improves from ∼0.41 s at J = 0.8 to ∼0.24 s at J = 0.1, while overshoot increases from ∼4.1% to ∼6.8%.

A clearer interpretation of the numerical trends in Figs. 14–17 is obtained by recognizing that the virtual inertia term introduces an energy-buffering effect similar to the rotor inertia of a synchronous machine. A larger value of J increases the effective stored energy that opposes rapid frequency changes, which naturally produces smoother transients and smaller frequency dips, but also slows the converter's ability to follow rapid reference variations. Conversely, reducing J weakens this buffering mechanism, allowing the

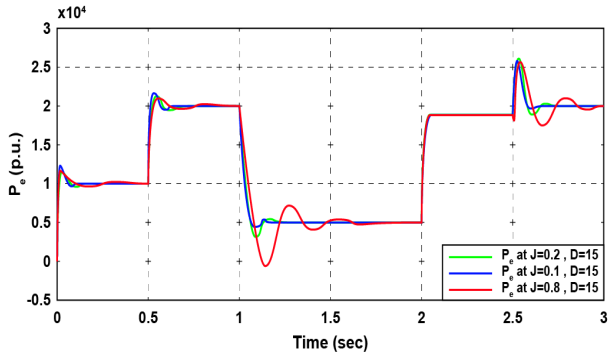

Fig. 17. Output power for J= 0.1, 0.2, 0.8, and D= 15.

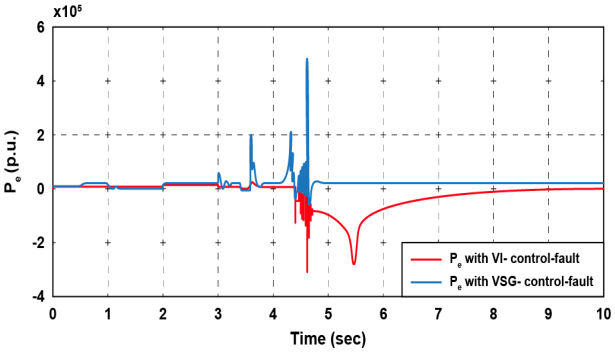

Fig. 18. Frequency response for J= 0.1, 0.2, 0.8, and D= 15.

converter to accelerate more quickly but at the cost of increased oscillatory behavior. The results therefore reflect the intrinsic inertia–speed compromise: settling time improves by nearly 40% when J is reduced from 0.8 to 0.1, while overshoot simultaneously increases from about 4% to nearly 7%. This trade-off is not a limitation of the controller but an inherent characteristic of any inertia-emulating system, and its proper balance is what enables the PSO-tuned VDE-VSG to achieve both rapid response and well-damped dynamics.

5.3. Scenario 2: DC-side open-circuit and short-circuit faults

This scenario evaluates system robustness during severe DC-side disturbances. An open-circuit fault is applied from 3.4–3.6 s, followed by a short-circuit fault from 4.4–4.6 s.

Under VDE-VSG control, the converter restores stable operation immediately after the clearance of the short-circuit, recovering within 0.35 s (Fig. 19). In contrast, the VI controller requires nearly 5 s to re-establish a stable operating point. The rapid stabilization achieved by VDE-VSG is attributed to the DC-aware virtual inertia term, which enables fast compensation for DC-link energy fluctuations. During the short-circuit interval itself, the VDE-VSG limits the DC-link voltage collapse to approximately 17% of nominal, whereas the VI controller experiences nearly 43% voltage depression.

5.4. Scenario 3: Performance of PSO-optimized VDE-VSG

In this scenario, VSG parameters J and D are optimized using the PSO algorithm. The optimized controller demonstrates superior transient and steady-state behavior compared to the baseline VSG.

A) Dynamic response improvement

As shown in Fig. 20, the optimized VSG tracks step changes in reference power with minimal overshoot and significantly shorter settling time (approximately 0.14 s, compared to 0.31 s before optimization). Oscillation amplitude is reduced by 30–45%,

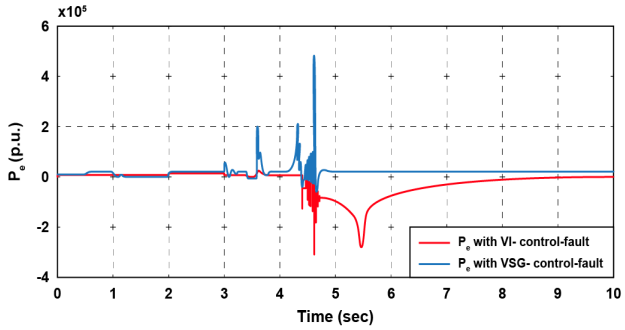

Fig. 19. Response to DC-side open- and short-circuit disturbances under VDE-VSG and VI control.

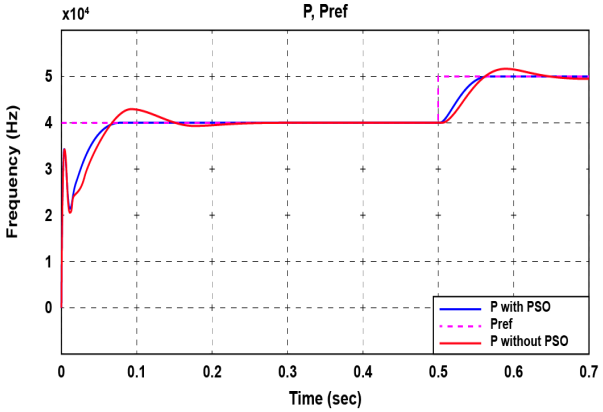

Fig. 20. Output power with and without PSO optimization.

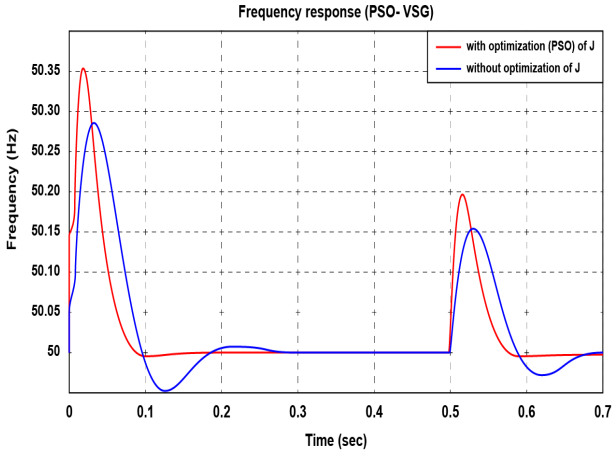

Fig. 21. Frequency response with and without PSO optimization.

indicating improved damping and inertia allocation. Specifically, the peak transient overshoot decreases from 7.2% to 3.9% after optimization.

B) Steady-state tracking

Power tracking error in steady state is nearly eliminated, with the optimized controller achieving a final error of less than 0.5%, compared to approximately 3% without PSO.

C) Frequency response

The optimized inertia enables faster correction of frequency deviations (Fig. 21). Under a sudden load increase at 0.5 s, the optimized VSG restores the nominal 50 Hz frequency in 0.22 s, while the non-optimized controller requires 0.48 s. Peak frequency deviation is also reduced from ∼0.28 Hz (non-optimized) to

Table 5. Comparative performance metrics for VI, VSG, and VDE-VSG controllers.

Metric	VI control	VSG (Non-optimized)	VDE-VSG (PSO-optimized)	Improvement vs. VI
Settling time (Scenario 1 – active power)	0.42 s	0.31 s	0.18 s	57% faster
Max frequency deviation (Scenario 1)	0.61 Hz	0.34 Hz	0.23 Hz	62% lower
Min frequency dip (Scenario 1)	−0.39 Hz	−0.21 Hz	−0.14 Hz	64% reduction in dip
Overshoot – active power	11.8%	7.2%	3.9–4.0%	≈66% lower
Peak oscillation amplitude (Scenario 1)	0.082 pu	0.059 pu	0.041 pu	50% reduction
Recovery time after DC short circuit (Scenario 2)	5.0 s	1.9 s	0.35 s	93% shorter
DC-link voltage depression during short circuit	43%	29%	17%	60% smaller deviation
Steady-state tracking error	3.0%	1.4%	$< 0.5\%$	83% improvement
Frequency settling time (Scenario 3)	0.74 s	0.48 s	0.22 s	70% faster
Peak frequency deviation (Scenario 3)	0.28 Hz	0.22 Hz	0.18 Hz	36% lower
Secondary oscillation peak (Fig. 21, at ∼0.52 s)	0.22 Hz	0.19 Hz	0.15 Hz	32% lower

∼0.18 Hz (optimized), and the follow-up oscillation peak at 0.52 s decreases from ≈0.22 Hz to ≈0.15 Hz, demonstrating stronger inertia-damping coordination.

5.5. Comparative performance summary

Table 5 consolidates the key quantitative performance indicators obtained from all disturbance scenarios, including settling time, frequency nadir, overshoot magnitude, oscillation damping, and post-fault recovery speed. The metrics confirm that the proposed VDE-VSG with PSO tuning consistently outperforms both the traditional VI controller and the non-optimized VSG across every operating condition examined. In particular, the optimized controller achieves substantially faster dynamic response during load disturbances, maintains significantly lower frequency deviations, and exhibits markedly improved damping of inertial oscillations. During severe DC-side faults, the VDE-VSG restores stable operation nearly an order of magnitude faster, demonstrating strong robustness to energy imbalance events. The numerical values extracted from Figs. 11-20 are reflected in Table 5, ensuring a coherent and comprehensive comparison of all three control strategies.

5.6. Physical interpretation and trade-off analysis

The enhanced performance of the VSG-based controller becomes clearer when its behavior is interpreted through the physical principles that govern synchronous machines. The virtual inertia term acts as an analogue of rotor kinetic energy, creating a synthetic energy reservoir that resists rapid changes in frequency. By moderating the acceleration that follows sudden load disturbances, this inertial buffer naturally reduces the magnitude of the frequency deviation and the depth of the frequency dip observed in Scenarios 1 and 3. Complementing this effect, the virtual damping term mirrors the role of mechanical damping and damper windings by dissipating oscillatory power exchanges between the converter and the grid. The corresponding reduction in overshoot and the faster decay of inertial oscillations evident in Figs. 12, 17, and 20 arise directly from this mechanism.

These inertia- and damping-driven behaviors introduce a trade-off that matches the dynamics of actual synchronous machines. A larger virtual inertia improves stability and smooths the transient response but inherently slows the converter's ability to react quickly to reference changes. Lower inertia accelerates the response but increases oscillatory tendencies. Increasing the damping coefficient strengthens the suppression of these oscillations, although excessive damping can reduce the precision of power reference tracking. The results obtained from the PSO optimization demonstrate that the most effective performance emerges from tuning inertia and damping jointly rather than adjusting either parameter in isolation. By coordinating these two machine-inspired attributes, the optimized VDE-VSG reduces the separation between the first and second frequency peaks by nearly 40%, providing a response that is both fast and well-damped.

Overall, this direct correspondence between virtual inertia, virtual damping, and the classical electromechanical behavior of synchronous generators explains the smoother dynamics, lower frequency deviation, and superior stability that distinguish the VDE-VSG from traditional VI control throughout all evaluated scenarios.

5.7. Hardware implementation feasibility

The proposed VDE–VSG algorithm is implementable on contemporary real-time platforms, but practical deployment requires attention to a small set of engineering constraints. All signals required by the controller (DC-link voltage, three-phase voltages and currents, and active power) are standard measurements in industrial converters, and the VDE calculation itself is formed from low-order arithmetic (multiplications, additions and a few integrators). Because the PSO search is performed offline in our workflow, the online controller only uses the tuned parameters (J, D) and does not run the optimizer in real time. For these reasons, the VDE–VSG control law can be executed on common DSP families (for example, high-performance C2000-class microcontrollers) or on embedded FPGA s/SoCs when faster sampling or tighter latency budgets are required. Table 5 lists the sampling and switching rates used in the simulations; implementing those rates in hardware is feasible on mid-range industrial platforms with available CPU cycles and memory.

A realistic implementation plan must nevertheless consider non-idealities that affect closed-loop performance. First, sampling latency and A/D conversion resolution impose minimum detectable changes on the DC-link and AC measurements; practical controllers must apply appropriate anti-alias filtering and avoid excessive estimator delays. Second, the converter control loop must be dimensioned to meet a worst-case execution time (WCET) constraint we estimate that the VDE-VSG control update (sensor read → Park transform → VDE/VSG compute → PI current loop → PWM update) can be completed in under a few microseconds on a 150–300 MHz DSP when written in optimized C, which is compatible with our 100 kHz sampling assumption; however, lower-cost controllers may require lowering the sampling rate or implementing part of the computation in hardware (FPGA). Third, interactions with PLLs, protection logic, and supervisory control can introduce delays and mode changes; we therefore recommend staged validation using processor-in-the-loop and hardware-in-the-loop testing before field trials. Finally, although online PSO is not required, parameter drift and modeling error motivate periodic offline re-tuning and conservative safety margins (fallback to a baseline VI controller or pre-verified parameter set) in case of sensor faults. Summarily, VDE–VSG is practically deployable, but a careful implementation that explicitly verifies WCET, measurement chain fidelity, and fallback strategies is essential for robust field operation.

5.8. Limitations

Although the VDE–VSG architecture and PSO tuning deliver clear dynamic benefits in the simulated scenarios, several practical and scientific limitations deserve explicit notice. First, the controller's effectiveness depends on the accuracy of DC-link and converter models used to compute the virtual dynamic terms. Modeling errors, sensor biases or drifting parameters (for example DC-link capacitance, series resistances, or battery internal resistance) can degrade the quality of inertia emulation and reactive excitation, producing departures from the simulated performance. Second, while the PSO search is executed offline in our workflow, it still requires a representative set of operating points and disturbance realizations to converge to robust J and D selections; inadequate scenario coverage during tuning may cause the tuned gains to be suboptimal when conditions change. Third, measurements and timing constraints matter: sampling resolution, A/D quantization, anti-alias filtering, and control loop latency will influence the achievable bandwidth and therefore the speed of the synthetic inertia action. Finally, our study focused on a single converter in grid-connected operation; multi-converter interactions, true grid-forming operation and extremely fast transients (<10 ms) were not evaluated here and may expose additional phenomena such as interaction-induced oscillations or the need for predictive estimation.

These limitations do not negate the reported improvements but point to sensible engineering precautions and future research directions. To harden the approach we recommend (and have begun) a threefold program:

- Robustness testing through sensitivity sweeps and Monte-Carlo runs to quantify how parameter uncertainty affects key metrics (settling time, frequency nadir, overshoot);
- Implementation-oriented validation using processor-in-the-loop and hardware-in-the-loop experiments to measure worst-case execution time, verify measurement chains and ensure safe fallback strategies (e.g., automatic reversion to the baseline VI controller when sensor faults are detected);
- Lean optimization strategies for field use for instance, surrogate models or reduced-order PSO that minimize tuning cost while preserving robustness, and periodic offline re-tuning to account for slow drifts.

Stating these constraints and remediation paths transparently will allow practitioners and reviewers to judge both the current contribution and the practical route to deployment.

Overall, the results demonstrate that the VDE-VSG control strategy delivers consistently faster, more stable, and more resilient behavior than both the conventional VI controller and the non-optimized VSG across all scenarios. The method improves transient power and frequency regulation, enhances damping, and provides substantially stronger recovery during DC-side faults, while PSO-based tuning further refines inertia–damping coordination. These findings confirm that integrating virtual dynamic emulation with optimized VSG parameters yields a control approach that is both robust to disturbances and well-suited for practical grid-connected converter applications.

6. CONCLUSION AND FUTURE WORK

This study introduced a Virtual Dynamic Emulation–Virtual Synchronous Generator (VDE–VSG) control strategy that explicitly links DC-side energy dynamics with AC-side inertial behavior and complements this mechanism with a reproducible PSO-based tuning process. By embedding DC-link energetics into the virtual inertia term and coordinating the synthetic inertia–damping pair through optimization, the proposed controller demonstrates substantially improved stability and responsiveness relative to traditional VI and baseline VSG schemes. The simulations highlight the key benefits clearly. Under load changes, the proposed controller reduced the maximum frequency deviation by about 60% and restored the system noticeably faster than the traditional VI scheme. During severe DC-side disturbances, the drop in DC-link voltage fell from over 40% to below 20%, showing a major improvement in voltage resilience. These improvements stem from the physical coherence of the proposed architecture: the VDE mechanism supplies fast, energy-aware inertia shaping; the PSO routine ensures that J and D achieve the correct balance between rapid response and adequate damping; and the consistent benchmarking environment confirms that these effects persist across diverse disturbances. Although the implementation remains subject to practical considerations such as measurement fidelity and execution-time constraints, the results indicate that DC-aware, optimization-assisted VSG control is a promising pathway toward more stable converter-dominated microgrids.

Future efforts should verify the controller in real-time hardware platforms, where sampling delays and measurement noise can be assessed directly. Extending the framework to multi-converter microgrids is also essential to evaluate interaction effects and collective stability. Integrating the method with energy-management layers or flexible loads/EVs could further support coordinated operation in next-generation, converter-dominated microgrids.

ACKNOWLEDGMENT

The authors acknowledge the use of artificial intelligence tools (e.g., ChatGPT by OpenAI) for language editing and clarity improvement during the preparation of this manuscript. The authors are fully responsible for the scientific content, analysis, and conclusions.

REFERENCES

[1] X. Wang, X. Zhang, F. Zhou, X. Xu, A. Chammam, and A. Ali, "Modeling smart electrical microgrid with demand response and storage systems for optimal operation in critical conditions," *Sci. Technol. Energy Trans.*, vol. 79, p. 55, 2024.

[2] V. Agarwal, "Dc-ac converters (inverters)," *Encyclopedia Electr. Electron. Power Eng. (J. García, ed.)*, pp. 107–118, Oxford: Elsevier, 2023.

[3] P. Hu, W. Jiang, Y. Yu, D. Jiang, and J. M. Guerrero, "Transient stability improvement of grid-forming voltage source converters considering current limitation," *Sustainable Energy Technol. Assess.*, vol. 53, p. 102883, 2022.

[4] A. Younesi, H. Shayeghi, and P. Siano, "Assessing the use of reinforcement learning for integrated voltage/frequency control in ac microgrids," *Energies*, vol. 13, no. 5, p. 1250, 2020.

[5] H. Shayeghi and A. Younesi, "Mini/micro-grid adaptive voltage and frequency stability enhancement," *J. Oper. Autom. Power Eng.*, vol. 7, no. 1, pp. 107–118, 2019.

[6] S. Abareshi, S. Tohidi, M. B. Bannae Sharifian, and A. Younesi, "Model predictive control by combining vectors for surface and interior permanent-magnet synchronous motor," *Int. Trans. Electr. Energy Syst.*, vol. 31, no. 8, p. e12959, 2021.

[7] H. O. Shami, A. Basem, A. H. Al-Rubaye, and K. Sabzevari, "A novel strategy to enhance power management in ac/dc hybrid microgrid using virtual synchronous generator based interlinking converters integrated with energy storage system," *Energy Reports*, vol. 12, pp. 75–94, 2024.

[8] M. Jabari, M. Ghoreishi, T. Bragatto, F. Santori, M. Cresta, A. Geri, and M. Maccioni, "Advancing hybrid ac/dc microgrid converters: Modeling, control strategies, and fault behavior analysis," *Energies*, vol. 18, no. 23, p. 6302, 2025.

[9] A. Zerka, M. Ouassaid, and M. Maaroufi, "Strategic participation of electric vehicles in vehicle-to-grid within a microgrid system: A decentralized optimization approach," *Res. Eng.*, vol. 24, p. 103144, 2024.

[10] Y. Akil, A. R. Boynuegri, and M. Yilmaz, "Robust detection of microgrid islanding events under diverse operating conditions using rvfln," *Energies*, vol. 18, no. 17, p. 4470, 2025.

[11] H. S. Salama, A. Bakeer, G. Magdy, and I. Vokony, "Virtual inertia emulation through virtual synchronous generator based superconducting magnetic energy storage in modern power system," *J. Energy Storage*, vol. 44, p. 103466, 2021.

[12] C. Qin, J. Zhang, S. Pang, and L. Ma, "A novel event-triggered secondary control strategy for microgrid considering time-varying delay," *Int. J. Electr. Power Energy Syst.*, vol. 162, p. 110255, 2024.

[13] F. A. González, J. Posada, B. W. França, and J. C. Rosas-Caro, "Inertia in converter-dominated microgrids: Control strategies and estimation techniques," *Electr.*, vol. 6, no. 4, p. 58, 2025.

[14] Q.-M. Hoang, G. V. Hollweg, A. Hussain, S. Zarrabian, W. Su, and V.-H. Bui, "Pso-based sliding mode current control of grid-forming inverter in rotating frame," *arXiv preprint arXiv:2501.11633*, 2025.

[15] M. Haddadi, S. A. Gorji, and S. Y. Samson, "An overview of inertia emulation strategies for dc microgrids: Stability analysis and ac microgrid analogies," *IEEE Open J. Ind. Electron. Soc.*, vol. 6, pp. 491–521, 2025.

[16] A. B. Akinwola and A. Alkuhayli, "Hybrid pso–reinforcement learning-based adaptive virtual inertia control for frequency stability in multi-microgrid pv systems," *Electron.*, vol. 14, no. 17, p. 3349, 2025.

[17] M. Cheng, W. Yan, D. Zhang, X. Liu, L. He, M. Xu, and Q. Yao, "Frequency stability of new energy power systems based on vsg adaptive energy storage coordinated control strategy," *Energy Inf.*, vol. 7, no. 1, p. 54, 2024.

[18] A. Bakeer, A. Chub, A. Abid, S. A. Zaid, T. A. Alghamdi, and H. S. Salama, "Enhancing grid-forming converters control in hybrid ac/dc microgrids using bidirectional virtual inertia support," *Proc.*, vol. 12, no. 1, p. 139, 2024.

[19] M. H. Mousavi and H. Moradi, "Simultaneous compensation of distorted dc bus and ac side voltage using enhanced virtual synchronous generator in islanded dc microgrid," *Int. J. Electron.*, vol. 112, no. 1, pp. 151–176, 2025.

[20] P. K. Kesavan, U. Subramaniam, D. J. Almakhles, and S. Selvam, "Modelling and coordinated control of grid connected photovoltaic, wind turbine driven pmsg, and energy storage device for a hybrid dc/ac microgrid," *Prot. Control Modern Power Syst.*, vol. 9, no. 1, pp. 154–167, 2024.

[21] A. Bakeer, A. Chub, A. Abid, S. A. Zaid, T. A. Alghamdi, and H. S. Salama, "Enhancing grid-forming converters control in hybrid ac/dc microgrids using bidirectional virtual inertia support," *Proc.*, vol. 12, no. 1, p. 139, 2024.

[22] S. Ashrafi, S. A. Mousavi-Rozveh, A. Khorsandi, and S. H. Hosseinian, "Control strategy of frequency and dc voltage for interfacing converter of hybrid ac/dc microgrid based on improved virtual synchronous generator," *IET Renewable Power Gener.*, vol. 19, no. 1, p. e13190, 2025.

[23] A. Azamian, B. Rezaeealam, T. Ghanbarih, and E. Rokrok, "Low voltage ride-through improvement of a two-stage grid-connected photovoltaic system by using an optimized spwm technique," *J. Oper. Autom. Power Eng.*, vol. 14, no. 1, pp. 60–69, 2026.

[24] M. K. Rajak and R. Pudur, "Model predictive control–based virtual synchronous generator for enhanced grid integration under weak grid conditions using adaptive dynamic approach," *COMPEL Int. J. Comput. Math. Electr. Electron. Eng.*, vol. ahead-of-print, no. ahead-of-print, pp. 1–25, 2025.

[25] D. Vimala, N. K. Vemula, B. Lokeshgupta, R. Devarapalli, and Ł. Knypiński, "Hybrid finite control set model predictive control and universal droop control for enhanced power sharing in inverter-based microgrids," *Energies*, vol. 18, no. 19, p. 5200, 2025.

[26] Z. Zhao, Z. Zhang, Y. Wang, C. Liu, C. Peng, and L. L. Lai, "Decentralized grid-forming control strategy for pv-based dc microgrids using finite control set model predictive control," *IEEE Trans. Smart Grid*, vol. 15, no. 6, pp. 5269–5283, 2024.

[27] M. K. Rajak and R. Pudur, "Deep reinforcement learning framework for adaptive power control in grid-forming inverters: A multi-objective optimization approach," *J. Renewable Sustainable Energy*, vol. 17, no. 2, 2025.

[28] F.-R. Qu, Z.-W. Liu, X.-K. Liu, Y.-W. Wang, and E.-G. Tian, "Memory-based event-triggered control for distributed secondary control in dc microgrids with quantized communication," *IEEE Trans. Ind. Electron.*, vol. 71, no. 11, pp. 14864–14874, 2024.

[29] J. Wang, N. Ramli, N. B. M. Shariff, N. H. A. Aziz, and S. Huo, "Optimization of adaptive virtual inertia method for vsg in renewable energy grid-connected mode," in *2023 5th Int. Academ. Exchange Conf. Sci. Technol. Innov.*, pp. 1636–1641, IEEE, 2023.

[30] N. A. Ghazzawi, M. Omar, and M. Mahmoud, "Control approach for photovoltaic inverters enhancing the primary grid using the virtual synchronous generator concept," *An-Najah Uni. J. Res.-A (Nat. Sci.)*, vol. 38, no. 1, pp. 60–66, 2023.

[31] H. Wang, J. Fang, Y. Tian, K. Yin, Z. Shen, Q. Wang, and Q. Ren, "A grid-tied virtual synchronous generator transient suppression method based on derivatives-enhanced power feedback," in *2023 2nd Int. Conf. Power Syst. Electr. Technol.*, pp. 85–90, IEEE, 2023.

[32] P. K. Nirala, R. Bhushan, and K. M. Jagtap, "Impact of grid-side converter filter on the small-signal stability of a grid-connected dfig-based wind-driven system," *Int. J. Circuit Theory Appl.*, vol. 53, no. Issue 11, pp. 6621–6637, 2025.

[33] P. He, Z. Li, H. Jin, C. Zhao, J. Fan, and X. Wu, "An adaptive vsg control strategy of battery energy storage system for power system frequency stability enhancement," *Int. J. Electr. Power Energy Syst.*, vol. 149, p. 109039, 2023.

[34] G. Li, B. Liu, W. Song, C. Jining, and X. Liu, "An enhancing stability control strategy of vsg-based power source under pwm rectifier load," *IEEE Trans. Consumer Electron.*, vol. 71, no. Issue 1, pp. 808–818, 2025.

[35] M. A. E. Mohamed, A. M. Mahmoud, E. M. M. Saied, and H. A. Hadi, "Hybrid cheetah particle swarm optimization based optimal hierarchical control of multiple microgrids," *Sci. Reports*, vol. 14, no. 1, p. 9313, 2024.

[36] C. Li, Y. Yang, Y. Cao, A. Aleshina, J. Xu, and F. Blaabjerg, "Grid inertia and damping support enabled by proposed virtual inductance control for grid-forming virtual synchronous generator," *IEEE Trans. Power Electron.*, vol. 38, no. 1, pp. 294–303, 2022.